

Region-based reconstruction method for fluorescent molecular tomography

Wei Zou,^{1,2,3} Jiajun Wang,^{1,2,3,*} and David Dagan Feng^{2,3,4}

¹*School of Electronics and Information Engineering, Soochow University, Suzhou 215021, China*

²*Department of Electronic and Information Engineering, Hong Kong Polytechnic University, Hong Kong*

³*School of Information Technologies, University of Sydney, Sydney, NSW 2006, Australia*

⁴*Med-X Research Institute, Shanghai Jiao Tong University, Shanghai 200030, China*

*Corresponding author: jjwang@suda.edu.cn

Received June 18, 2010; revised August 23, 2010; accepted August 24, 2010;
posted August 24, 2010 (Doc. ID 130341); published September 29, 2010

A common difficulty for the traditional methods of fluorescent molecular tomographic (FMT) reconstruction is that only a small amount of measurements can be used to recover the image comprised of a large number of pixels. This difficulty not only leads to expensive computational cost but also likely results in an unstable solution prone to be affected by the noise in the measurement data. In this paper, we propose a region-based method for reducing the unknowns, where the target areas are determined by searching for the nearest neighbor nodes. In this method, the Hessian matrix of the second-order derivatives is incorporated to speed up the optimization process. An iteration strategy of multi-wavelength measurement is introduced to further improve the accuracy of inverse solutions. Simulation results demonstrate that the proposed approach can significantly speed up the reconstruction process and improve the image quality of FMT. © 2010 Optical Society of America
OCIS codes: 100.3190, 170.3010, 170.3880, 170.6960, 260.2510.

1. INTRODUCTION

It is well known that the biological tissues have relatively low optical absorption in the near-infrared (NIR) spectral window, which has enabled a variety of NIR imaging techniques [1,2]. The use of low-energy photons yields no radiation hazard and requires cost-effective instrumentation. In recent years, fluorescent molecular tomography (FMT) has emerged as a promising tool for small animal imaging due to its ability to offer noninvasive tomographic reconstruction of cellular and subcellular function in tissues [3]. FMT is an optical imaging technique for depth-resolved imaging of fluorescent-tagged objects. In this imaging modality, the injected fluorophore usually accumulates in diseased tissue as a result of the increased vascular density or by means of selective targeting [4]. A laser emits photons at the excitation wavelength. These photons propagate through the tissue and undergo absorption and scattering events. The fluorophore absorbs the excitation light and then decays to the ground state while releasing the energy, which is detected as fluorescence. The emitted photon has a longer wavelength than that of the excitation photon, resulting in a color shift. From the measured data, one can reconstruct the images of the fluorescent lifetime and the fluorescent yield [5].

Reconstruction of FMT involves the generation of a forward model that predicts the observable states at the measurement sites based on the known excitation light sources and the spatial distributions of optical properties of the tissue [6]. In addition to the forward model, fluorescence tomography in tissues also requires an inverse method to reconstruct interior optical and fluorescent property maps of the tissue from noisy measurements [7]. Basically, the inverse problem of FMT can be solved with

solutions of the forward model obtained either numerically or analytically [8].

It is generally accepted that one of the major challenges in image reconstruction is the high computational complexity. A common difficulty with the traditional methods is that only a small amount of data from measurements can be used to recover the image comprised of a large number of unknown parameters. Large-scale tomographic reconstructions not only bring a heavy computational burden, but also lead to a low precision of the inverse solutions due to the ill-posedness of the problem. In order to reduce the number of unknowns for improving the ill-posed nature of the inverse problem, and hence for improving the reconstructed results, some related researches have been conducted. In [9], a model-order reduction (MOR) technique is adopted to reduce the system complexity, where instead of solving the full-order model system involving thousands of state variables, the unknowns are expressed in the subspace with a reduced dimension. In this method, the Wilson–Yuan–Dickens (WYD) basis vectors or the Lanczos basis vectors in the Krylov subspace are used to construct a transformation matrix. In [10], an efficient technique for direct object localization and characterization is proposed, where the number of unknowns is reduced by appropriate parameterization as well as the B-spline model. The computational advantage of that method is its inherent parallelism. However, that work is concerned with the problem with only one target included. Kolehmainen *et al.* also made an important contribution by proposing another method for the same purpose, where the diffusion equation with piecewise constant decay and diffusion coefficients is employed to model the forward problem [11].

That approach is proposed only for the recovery of the region boundaries on the basis of the necessary assumption that the values of the diffusion and decay coefficients are known *a priori*.

The aim of our work is to improve the quality of the reconstructed image as well as speed up the reconstruction process of the FMT. Based on the previous research, in this paper, an innovative region-based method without the need of that prior information is proposed for reduction of unknowns in the FMT reconstruction. Because fluctuations in properties of the interior of a region are usually much smaller than the differences between the background and targets or between the different targets, the proposed method classifies the image to be reconstructed into two different kinds of areas (background and target areas) and then assigns constant value to the property in the interior of a region. This can lead to a significant reduction of the unknowns involved in the reconstruction. In this method, the target areas are constructed by attaching to each target its nearest neighbor node with minimum cost one by one from the background region. The proposed region-based reconstruction method converts a highly underdetermined problem of reconstructing an image with a large number of pixels to a well determined problem of reconstructing the target regions and the background area with constant optical properties for each area. As compared with other methods proposed in the literature, the most important innovation of our proposed method lies in the fact that it can deal with problems with multiple target areas of anomalies. In addition, different from the traditional iterative reconstruction algorithms, where only the first-order derivatives are involved, we propose to incorporate the second-order derivatives (i.e., the Hessian matrix) in the iterative optimization problem to further improve the reconstruction accuracy, as well as to accelerate the reconstruction process. A multi-wavelength reconstruction strategy that employs the excitation and emission light measurements is also proposed to improve the quality of the reconstructed results. Simulation results demonstrate that both the speed and precision of the reconstruction can be significantly improved with our proposed algorithm.

2. METHODS

A. Forward Diffusion Modeling

Propagation of photons in biological tissue is basically governed by the radiative transfer equation (RTE). However, the use of RTE is computationally expensive in biomedical imaging. An alternative simplification approach is the diffusion approximation [12]. The diffusion equation approximates the photon propagation under the assumption that scatter dominates over absorption [13]. The generation and propagation of fluorescence light through highly scattering is often modeled by a pair of partial differential equations. In the frequency domain, the propagation of excitation light over a bounded domain Ω at a given modulation frequency is described by the following diffusion equation:

$$-\nabla \cdot (D_x \nabla \Phi_x) + k_x \Phi_x = S_x \quad \text{on } \Omega, \quad (1)$$

where the subscript x denotes the measurements or properties at the excitation wavelength λ_x , ∇ is the gradient

operator, $S_x(\text{W}/\text{cm}^3)$ is the excitation light source whose intensity is usually modulated on a sinusoidal signal, $\Phi_x(\text{W}/\text{cm}^2)$ is the photon fluence at the excitation wavelength, $D_x(\text{cm})$ is the optical diffusion coefficient, and $k_x(\text{cm}^{-1})$ is the decay coefficient.

The generation and propagation of the emission light can be described in a manner similar to that of the excitation light:

$$-\nabla \cdot (D_m \nabla \Phi_m) + k_m \Phi_m = S_m = \varphi \mu_{axf} \frac{1 + i\omega\tau}{1 + (\omega\tau)^2} \Phi_x \quad \text{on } \Omega. \quad (2)$$

The subscript m denotes the parameters or measurements at the emission wavelength λ_m , $\Phi_m(\text{W}/\text{cm}^2)$ is the photon fluence at the emission wavelength, S_m is the emission light source, φ is the fluorescence quantum efficiency, $\tau(s)$ is the fluorescence lifetime, and $i = (-1)^{1/2}$. The diffusion coefficient $D_{x,m}(\text{cm})$ and the decay coefficient $k_{x,m}(\text{cm}^{-1})$ are defined as follows:

$$D_{x,m} = \frac{1}{3(\mu_{ax,mi} + \mu_{ax,mf} + \mu'_{sx,m})}, \quad (3)$$

$$k_{x,m} = \frac{i\omega}{c} + \mu_{ax,mi} + \mu_{ax,mf}, \quad (4)$$

where $\mu_{ax,mi}(\text{cm}^{-1})$ is the absorption coefficient due to the nonfluorescing chromophore, $\mu_{ax,mf}(\text{cm}^{-1})$ is the absorption coefficient due to the fluorophore, $\mu'_{sx,m}(\text{cm}^{-1})$ is the isotropic scattering coefficient, $\omega(\text{rad}/s)$ denotes the angular modulation frequency of the excitation light source [14], and $c(\text{cm}/s)$ is the speed of light in the medium.

The forward solver obtains the fluence for a given distribution of optical and fluorescent properties by applying suitable boundary conditions such as the following Robin-type boundary conditions:

$$\mathbf{n} \cdot (D_x \nabla \Phi_x) + b_x \Phi_x = 0 \quad \text{on } \partial\Omega, \quad (5)$$

$$\mathbf{n} \cdot (D_m \nabla \Phi_m) + b_m \Phi_m = 0 \quad \text{on } \partial\Omega, \quad (6)$$

where \mathbf{n} is the vector normal to the boundary $\partial\Omega$. The Robin boundary coefficients b_x and b_m are governed by the reflection coefficients R_x and R_m , respectively [15].

The forward Eqs. (1) and (2) can be solved with analytical methods [16] or numerical methods such as the finite element method (FEM) [17]. The analytical method is more computationally efficient, but simplified assumptions of geometry and properties may lead to inaccurate results [18]. The most important superiority of FEM is its versatility, which makes it applicable to complex geometries and highly inhomogeneous property distributions. In this study, the FEM is employed to solve the forward model. We give here a brief introduction of forming the FEM equations for the forward problem. The domain Ω is first partitioned into M non-overlapped elements Ω_i ($i = 1, 2, \dots, M$) joined at N vertex nodes, such that $\Omega = \cup_{i=1}^M \Omega_i$. Let $\Phi_{x,m} \approx \sum_{i=1}^N \Phi_{xi,mi} \phi_i$ be an N -node finite-element discretization of the photon fluence with basis

functions $\phi = \{\phi_i, i=1, 2, \dots, N\}$. Thus, the diffusion equations in the FEM framework can be expressed as the following matrix form [19]:

$$\mathbf{A}_x \Phi_x = \mathbf{S}_x, \quad (7)$$

$$\mathbf{A}_m \Phi_m = \mathbf{S}_m, \quad (8)$$

where the entries of matrices $\mathbf{A}_{x,m}$ and $\mathbf{S}_{x,m}$ can be given, respectively, by

$$A_{ij} = \int_{\Omega} \int_{\Omega} D_{x,m} \nabla \phi_i \cdot \nabla \phi_j d\Omega + \int_{\Omega} k_{x,m} \phi_i \phi_j d\Omega + \int_{\partial\Omega} b_{x,m} \phi_i \phi_j ds, \quad (9)$$

$$S_i = \int_{\Omega} S_{x,m} \phi_i d\Omega. \quad (10)$$

B. Linear Reconstruction

The forward problem is to predict the measurements y from a given distribution of tissue parameters x and the light sources, which can be represented by a nonlinear forward operator

$$y = F(x), \quad (11)$$

where F is the forward operator.

Similarly, in the inverse problem, the task is to derive the tissue parameter distribution x on the basis of the known distribution of the light sources and the measurements y . Generally, y is a nonlinear function of x . To simplify the problem, the function F can be expanded in the vicinity of x_0 in a Taylor series as [20]

$$y = F(x_0) + F'(x_0)(x - x_0) + \frac{1}{2!} F''(x_0)(x - x_0)^2 + \dots + \frac{1}{n!} \times F^{(n)}(x_0)(x - x_0)^n + \dots, \quad (12)$$

where F' , F'' , and $F^{(n)}$ are the first-, second-, and n th-order Frechet derivatives of F , respectively.

The extent of accuracy of the Taylor approximation is controlled by the residual term. In traditional image reconstruction algorithms, only up to the first-order derivatives are usually kept for the aforementioned approximation in Eq. (12), which results in the following linearized approximation:

$$y = F(x_0) + F'(x_0)(x - x_0). \quad (13)$$

The solution to Eq. (13) can be expressed in a matrix form:

$$\Delta \mathbf{x} = (\mathbf{J}^T \mathbf{J} + \lambda \mathbf{I})^{-1} \mathbf{J}^T \Delta \mathbf{y}, \quad (14)$$

where the Jacobian matrix $\mathbf{J} \in \mathbb{R}^{M \times N}$, with M and N being, respectively, the number of measurements and vertex nodes, is the matrix form of the Frechet derivatives F' . It is usually referred to as the first-order sensitivity matrix. The vectors $\Delta \mathbf{x} \in \mathbb{R}^N$ are the perturbations in the optical or fluorescent properties, while $\Delta \mathbf{y} \in \mathbb{R}^M$ is the residual data between the measurements and the predicted data.

The second term in the parentheses is the Tikhonov regularization term for tackling the ill-posedness of the inverse problem.

Solving Eq. (14) involves computing a matrix inversion of $(\mathbf{J}^T \mathbf{J} + \lambda \mathbf{I})^{-1}$, which is computationally expensive because the dimension of that matrix $N \times N$ is usually extremely large. To reduce the computational intensity while considering the fact that the value of N is usually much larger than that of M , the strategy proposed in [21] will be adopted here. Following this idea, Eq. (14) can be rewritten as follows:

$$\Delta \mathbf{x} = \mathbf{J}^T (\mathbf{J} \mathbf{J}^T + \lambda \mathbf{I})^{-1} \Delta \mathbf{y}. \quad (15)$$

Different from that in Eq. (14), the matrix to be inverted in Eq. (15) is $\mathbf{J} \mathbf{J}^T + \lambda \mathbf{I}$ with a size of $M \times M$ which is much smaller than $N \times N$, and hence the computational intensity can be significantly reduced.

C. Reconstruction Based on the Second-Order

Sensitivity Matrix

Basically, linear approximation is usually employed in the traditional reconstruction of FMT. The reason for neglecting the second- and other even higher-order derivatives is their extremely high computational complexity when involved in the iterative reconstruction, especially for large-scale reconstruction. However, involving the higher-order derivatives in the reconstruction process will be helpful to improve the convergence property of the algorithms. Therefore, if the scale of the inverse problem or the number of unknowns to be reconstructed can be reduced, it will be possible to introduce the second-order derivatives into the inverse problem for improving the efficiency of reconstruction with low computational requirements. As pointed out in the introduction, the number of unknowns will be reduced by using a region-based reconstruction method instead of the pixel-based one. Hence, the second-order derivatives will be employed in our reconstruction.

To derive the framework for the nonlinear reconstruction of FMT with the second-order derivatives involved, the inverse problem is described as the following optimization problem:

$$\mathbf{x} = \arg \min_{\mathbf{x}} \psi(\mathbf{x}) = \|\mathbf{y} - F(\mathbf{x})\|^2 + \lambda \|\mathbf{x}\|^2, \quad (16)$$

where $\psi(\mathbf{x})$ is a multi-variable objective function with $\mathbf{x} = [x_1, x_2, \dots, x_N]^T$, the second term on the right-hand side (RHS) of Eq. (16) is the regularization term to improve the ill-posedness of the reconstruction, λ is the regularization parameter, and $\|\cdot\|$ is the L_2 -norm.

We expand the above objective function in the vicinity of \mathbf{x} in a Taylor series and keep up to the first- and second-order terms as follows:

$$\psi(\mathbf{x} + \Delta \mathbf{x}) = \psi(\mathbf{x}) + [\nabla \psi(\mathbf{x})]^T \Delta \mathbf{x} + \frac{1}{2} \Delta \mathbf{x}^T \mathbf{H} \Delta \mathbf{x}, \quad (17)$$

where the vector $\Delta \mathbf{x}$ is the perturbation in the optical or fluorescent properties, and $\nabla \psi(\mathbf{x})$ is the gradient of the objective function at \mathbf{x} , i.e.,

$$\nabla \psi(\mathbf{x}) = \begin{bmatrix} \frac{\partial \psi(\mathbf{x})}{\partial x_1} & \frac{\partial \psi(\mathbf{x})}{\partial x_2} & \cdots & \frac{\partial \psi(\mathbf{x})}{\partial x_N} \end{bmatrix}^T. \quad (18)$$

\mathbf{H} is the Hessian matrix (also referred to as the second-order sensitivity matrix), whose entries are the second-order partial derivatives of the objective function with respect to all unknown parameters \mathbf{x} describing the local curvature of the objective function with respect to many variables [22]. Let $\psi: \mathbb{R}^N \rightarrow \mathbb{R}$, be a real-valued function as defined above; then the $N \times N$ Hessian matrix \mathbf{H} can be obtained as

$$\mathbf{H} = \begin{bmatrix} \frac{\partial^2 \psi}{\partial x_1^2} & \frac{\partial^2 \psi}{\partial x_1 \partial x_2} & \cdots & \frac{\partial^2 \psi}{\partial x_1 \partial x_N} \\ \frac{\partial^2 \psi}{\partial x_2 \partial x_1} & \frac{\partial^2 \psi}{\partial x_2^2} & \cdots & \frac{\partial^2 \psi}{\partial x_2 \partial x_N} \\ \vdots & \vdots & \ddots & \vdots \\ \frac{\partial^2 \psi}{\partial x_N \partial x_1} & \frac{\partial^2 \psi}{\partial x_N \partial x_2} & \cdots & \frac{\partial^2 \psi}{\partial x_N^2} \end{bmatrix}. \quad (19)$$

Suppose that the objective function ψ attains its extremum at $\mathbf{x} + \Delta \mathbf{x}$; hence the iterative expression for the inverse problem of FMT based on the second-order sensitivity matrix can be obtained as

$$\mathbf{H} \Delta \mathbf{x} = -\nabla \psi(\mathbf{x}). \quad (20)$$

D. Region-Based Reconstruction

As mentioned before, the inverse problem of FMT reconstruction is ill-posed. The ill-posedness may be due to its intrinsic properties or lack of enough measured data. For an ill-posed problem, small variations in the data will result in large changes in the solution, i.e., the solution is not stable and is sensitive to noise [23].

There are some ways to tackle the ill-posedness of the inverse problem. One of such methods is to incorporate the prior information into the inverse problem. Such prior information can either be obtained from other imaging modalities [24] or be incorporated in a manner by introducing penalty functions, as well as regularization terms such as in Eq. (14) [25,26]. An alternative way of improving the ill-posed nature of the FMT reconstruction is to reduce the number of unknowns involved in the reconstruction. Extremely large numbers of unknown parameters not only result in the ill-posed nature, but also increase the complexity and the computational intensity of the reconstruction problem. Therefore, it will be of great value to reduce the number of unknowns while not reducing the image quality. For such a purpose, some strategies have been proposed in the literature [9–11]. In this paper, we propose to reduce the number of unknowns in FMT reconstruction by classifying the image into two different kinds of areas (background and target areas) and assigning a constant value to the property in the interior of a region. Such a region-based reconstruction method tries to convert a highly underdetermined problem of reconstructing an image with a large number of pixels to a well-determined problem of reconstructing the target regions and the background area with constant optical properties for each area. This is plausible because the

fluctuations in properties of the interior of a region are usually much smaller than the differences between the background and targets or between the different targets. Because of the significant reduction of the number of unknowns that need to be reconstructed, not only the ill-posedness of the problem can be improved, but also the reconstruction process can be accelerated. As compared with previous region-based algorithms, the most important innovation of our proposed method lies in the fact that it can deal with problems with multiple target areas of anomalies, which are not unusual in medical imaging.

The first task of our method is to determine the number of targets and their centers, which is of critical importance for image reconstruction. Basically, different targets have different properties. Furthermore, the number of the targets is really important in clinical application for diagnosis and therapy. In our approach, the number of target regions as well as the initial target centers are estimated from the initial guess obtained using the traditional reconstruction method as illustrated in Eq. (15). Pixels with the extremum value in the areas of refined grids generated as discussed in Subsection 2. E will be assumed as the initial centers of the target areas. Obviously, the number of targets can be easily determined by counting the number of centers just obtained. After determining the number of target regions and their centers, different constants will be assigned to the properties of the background and the targets regions. Thus, the traditional pixel-based reconstruction problem with a large number of unknowns involved can be converted to the region-based reconstruction with only a small number of unknowns corresponding to the background and targets, which can be more efficiently solved.

The next task is to reconstruct the regions from the initial estimated centers. In our algorithm, the target areas will grow gradually along with the evolution of the iterative process. Suppose that the number of target regions determined from the initial guess is q , and the nodes of the triangular grid in the whole reconstructed area are denoted by p_i ($i=1, 2, \dots, N$) with N being the number of nodes. Initially, only the centers are assumed as the targets and the rest of the areas are assumed to be the background. The algorithm proceeds by attaching to each target its nearest neighbor node with the minimum cost from the background region. The cost of a node is defined as the discrepancy between the measured and the predicted data if the node is attached to the center. Such a cost can be computed by two steps: first, the iterative reconstruction as in Eq. (20) is implemented with the assumption that the node under consideration is attached to the center; second, the cost of the node is computed using the objective function as in Eq. (16) with the reconstruction result just obtained in the first step as an input. Here, the nearest neighbor nodes are defined based on the two-dimensional Euclidean distance:

$$b_k = \min_{i=1,2,\dots,N} \|p_i - c_k\|, \quad (21)$$

$$\|p_i - c_k\| = \sqrt{(x_{p_i} - x_{c_k})^2 + (y_{p_i} - y_{c_k})^2}, \quad (22)$$

where c_k ($k=1, 2, \dots, q$) is the k th center, b_k is its nearest neighbor node, x_{p_i} and x_{c_k} are the x coordinate of the

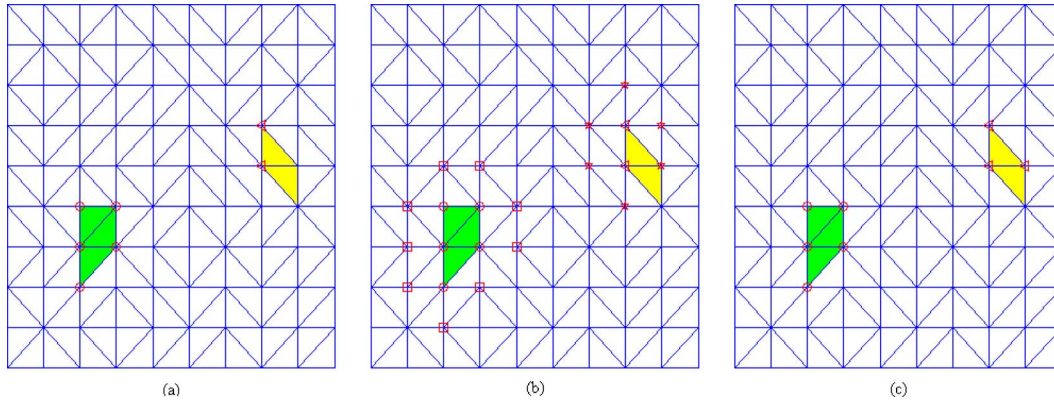


Fig. 1. (Color online) Schematic illustration of the process of target area growth. (a) Existing target nodes that have been found, (b) the nearest neighbor nodes of the existing target nodes, and (c) the candidate node with the minimum cost is attached as the target node.

points p_i and c_k , respectively, and y_{p_i} and y_{c_k} represent the y coordinates of p_i and c_k . The nearest neighbor nodes as defined above are only candidate nodes for being attached to the target. After computing the cost for each nearest neighbor node, only those with the minimum cost will be chosen and attached. Such a process is repeated until some stopping criteria are satisfied. The process of the target area growth is schematically illustrated in Fig. 1. The circles and triangles denote the existing target nodes that have been found in the shaded (green online) target area on the left and the shaded (yellow online) target area on the right, respectively [see Fig. 1(a)]. The squares and pentagams represent the corresponding nearest neighbor nodes of the existing target nodes that will be selected as the candidate nodes (see Fig. 1(b)) for attachment. Only the candidate node with the minimum cost is chosen as the target node (see Fig. 1(c)). The overall reconstruction algorithm can be summarized as follows:

1. the initial guess \mathbf{x}_l is obtained using Eq. (15), set $l = 0$;
2. for each target center c_k , choose the nearest neighbor node b_k from Eq. (21) and attach them to the targets;
3. for each node in the target areas, the nearest neighbor nodes are chosen one by one as the candidate nodes (including the nearest neighbor nodes with the same distance), which forms the new possible target regions;
4. the reconstruction is implemented based on the second-order derivative as in Eq. (20) for the new possible target regions generated in step 3. Evaluate the cost using the objective function as in Eq. (16);
5. the targets are updated by attaching the candidate node with the minimum cost to the original targets, $\mathbf{x}_l = \mathbf{x}_{l+1}$, let $l = l + 1$;
6. if $\psi(\mathbf{x}_l) > \varepsilon$ (defined termination criterion ε) go to 3; else output \mathbf{x}_l .

E. Adaptively Refined Grid Generation

The accuracy of FEM solutions of differential equations depends on the grid size [27]. Thus the accuracy of reconstructed results can be improved by decreasing the grid size. However, a global fine grid will increase the ill-posedness of the reconstruction and result in unacceptable computational requirements because of the increased number of unknowns. To tackle the above problem with-

out significantly reducing the image resolution, we propose to reconstruct the image based on an adaptively refined grid.

Because of the relatively higher spatial resolution of the structural imaging modalities, such as X-ray computerized tomography and magnetic resonance imaging (MRI), it will be helpful to improve the reconstructed image quality and accelerate the reconstruction process if the structural image is used as the prior information for grid generation. In structural imaging, areas with large variations in pixel values, which are likely to be edges between different tissues or between normal and abnormal tissues, should be reconstructed with high resolution, whereas regions with small variations, which are likely to lie in the interior of the tissues, can be reconstructed with low resolution, which will not affect the quality of the reconstructed image. Following this idea, the reconstructed domain is first uniformly discretized according to the Delaunay triangulation scheme, after which the uniform grid is refined only for the areas with large variations in pixel values. For an area, whether the grid needs to be refined can be judged by the corresponding variations of the pixel values in the triangle in the structural tomography, i.e.,

$$D(X) = E\{[X - E(X)]^2\}, \quad (23)$$

where X is the pixel value in the triangular unit in the prior image, E is the expectation operator, and D is the variation of pixel values in the triangle. When the variation is larger than the assumed threshold, the corresponding triangle will be divided further to obtain higher resolution. With such a variation, adaptive meshing can be realized, in which triangles in the regions with large variations will be further segmented into finer triangles to achieve high resolution.

In addition, such a strategy of adaptive grid refining will be helpful to locate the target regions in the proposed algorithm. On the one hand, when we are searching for the nearest neighbor nodes of the target areas to form the new updated target regions, the nodes located in the refined area are most likely to be chosen due to their nearest distances to each other. Hence, the refined areas generated based on the prior information are the possible target areas, which can help locate the targets in a correct

direction. On the other hand, in the possible background area, the grid is not refined and the resolution is relatively low. This can accelerate the searching process of targets.

3. RESULTS AND DISCUSSION

In our current implementation, we will focus on reconstructing the distribution of absorption coefficient μ_{axf} due to the fluorophore. Actually, two kinds of photons at different wavelengths are involved in the process of FMT image reconstruction. We can see that the quantity μ_{axf} is contained in both of Eqs. (1) and (2). Basically, in step 4 of the proposed algorithm, the single property in FMT is reconstructed based on only one kind of measurements, that is, from either the excitation or emission light wavelength. In this paper, an iteration scheme based on multi-wavelength measurements is proposed to reconstruct the distribution of absorption coefficient, i.e., two types of measurements were adopted: measurements from both emission and excitation light. This strategy is motivated by the fact that two types of measurements from different wavelengths can provide more information than only one kind of measurement from a single wavelength during the iteration process, and hence the quality of reconstructed results can be improved. In addition, the iterative results from one kind of measurement can provide a good initial guess for the next iteration with the other kind of mea-

surements. As a result, the precision of solutions can be improved using this multi-wavelength measurement strategy.

This scheme is also suitable for the case of other elements contained in Eq. (1). Two kinds of measurements are used in turn for iteration in the proposed multi-wavelength measurement scheme. The iterative result from the excitation light measurement is used as an input to the iteration of the emission light measurement, whose result is then used in turn as an input to the former. The process runs repeatedly until the cost can no longer be reduced or some convergence criteria are achieved. Figure 2 shows the iteration strategy of multi-wavelength-measurement-based reconstruction schematically for step 4 of the proposed algorithm.

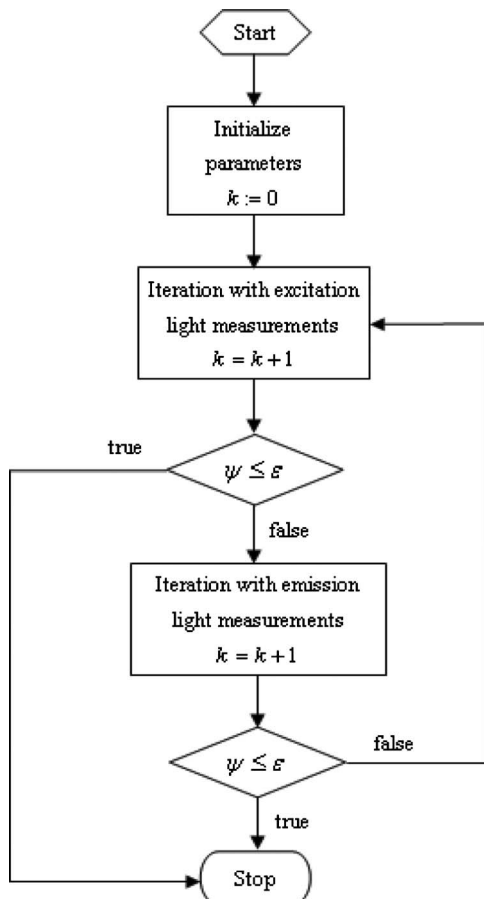


Fig. 2. Flow diagram for the multi-wavelength measurement scheme.

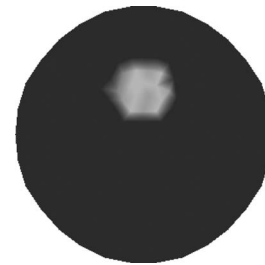


Fig. 3. Simulated phantoms for FMT of single target phantom.

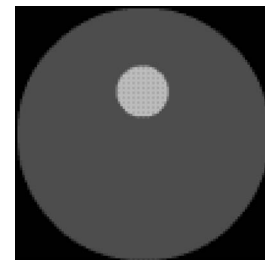


Fig. 4. Model of prior image of single target phantom.

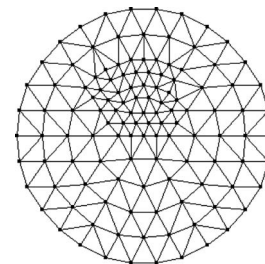


Fig. 5. Adaptively refined grid of single target phantom.

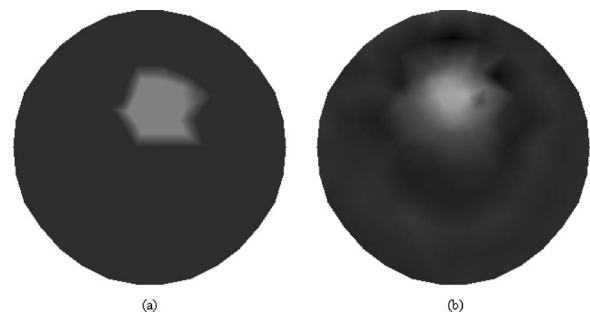


Fig. 6. Reconstructed image of absorption coefficient due to fluorophore μ_{axf} of single target phantom. (a) Proposed algorithm and (b) traditional method.

Table 1. Optical and Fluorescent Properties of Single Target Phantom

Excitation Light	$\mu_{axf}(\text{mm}^{-1})$	$\mu_{axi}(\text{mm}^{-1})$	$\mu'_{sx}(\text{mm}^{-1})$	φ	$\tau(\text{ns})$
Background	0.01	0.06	4.0	0.2	0.5
Target	0.15	0.06	4.0	0.2	0.5
Emission Light	$\mu_{amf}(\text{mm}^{-1})$	$\mu_{ami}(\text{mm}^{-1})$	$\mu'_{sm}(\text{mm}^{-1})$	φ	$\tau(\text{ns})$
Background	0.006	0.02	1.0	0.2	0.5
Target	0.1	0.02	1.0	0.2	0.5

Table 2. Performance Comparison for Algorithms of Single Target Phantom

Performance	Proposed Algorithm	Traditional Method
MSE	3.861×10^{-4}	4.792×10^{-4}
Averaged absolute value of relative error	2.129×10^{-2}	2.325×10^{-2}
Computation time (s)	149	217

The performance of the proposed approach is evaluated using the simulated data. The simulated forward data are obtained from Eqs. (1) and (2) in which Gaussian noise with a signal-to-noise ratio of 10 dB is added to evaluate the noise robustness of the algorithms. In the first set of simulations, a single fluorescent target is contained in the phantom, while in the second set of simulations, double targets are employed.

A. Single Fluorescent Target

The validation of the proposed algorithm is first performed on a 2-D circular domain as shown in Fig. 3, which contains one target representing the fluorescence center. Table 1 outlines the optical and fluorescent parameters in different regions of the simulated phantom. Four sources and thirty detectors are positioned alternately around the circle with equal intervals between each.

We employ the image shown in Fig. 4 with a resolution of 100×100 pixels as the prior image corresponding to Fig. 3. The grid with 122 nodes and 212 triangular elements is generated as shown in Fig. 5. The grid is refined around the reconstructed target while the other area is left with the coarse resolution.

Figures 6(a) and 6(b) illustrate the reconstructed images of μ_{axf} using the proposed algorithm and the tradi-

tional pixel-based method, respectively. We note that the traditional method reconstructs the anomaly with an incorrect size (larger than it should be), while the proposed algorithm can give a more accurate location and contour of the anomaly.

For the convenience of further evaluating the performance of the reconstruction algorithms, both the mean square error (MSE) of μ_{axf} and the relative error as defined in Eqs. (24) and (25), respectively, are introduced:

$$\text{MSE} = \frac{1}{N} \sum_{i=1}^N (\tilde{p}_i - p_i)^2, \quad (24)$$

$$r_i = \frac{(p_i - \tilde{p}_i)}{\tilde{p}_i} \times 100\%, \quad i = 1, 2, \dots, N, \quad (25)$$

where N is the number of vertex nodes, and \tilde{p}_i and p_i are the original pixel and reconstructed pixel values, respectively.

The performance of the two algorithms in terms of the computation time, the MSE, and the averaged absolute value of the relative error is summarized in Table 2 for comparison in detail, which shows a significant computation reduction of the proposed algorithm over the traditional method. It can also be observed that the quality of reconstruction is improved using the proposed algorithm.

To illustrate the superiorities of the iteration scheme based on multi-wavelength measurement, both reconstructed images of μ_{axf} based on the single and multi-wavelength measurement are shown in Fig. 7, with (a), (b), and (c) corresponding, respectively, to the results with the excitation light, the emission light, and the multi-wavelength measurement. Reconstructed results indicate that making use of single wavelength measurement for image reconstruction likely results in an incorrect shape

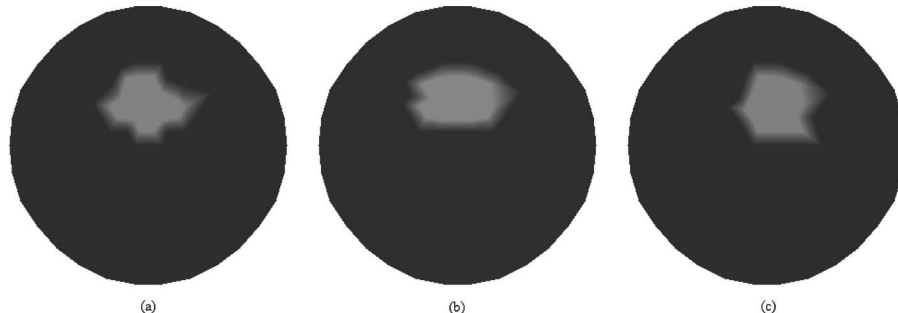


Fig. 7. Reconstructed image of absorption coefficient due to fluorophore μ_{axf} of single target phantom. (a) With excitation light measurement, (b) with emission light measurement, and (c) with multi-wavelength measurement.

Table 3. Performance Comparison for Reconstructed Results of Single Target Phantom Based on Different Kinds of Measurement

Performance	Reconstruction with Excitation Light Measurement	Reconstruction with Emission Light Measurement	Reconstruction with Multi-Wavelength measurement
MSE	4.359×10^{-4}	4.273×10^{-4}	3.861×10^{-4}
Averaged absolute value of relative error	2.284×10^{-2}	2.236×10^{-2}	2.129×10^{-2}

Table 4. Optical and Fluorescent Properties of Double Target Phantom

Excitation Light	$\mu_{axf}(\text{mm}^{-1})$	$\mu_{axi}(\text{mm}^{-1})$	$\mu'_{sx}(\text{mm}^{-1})$	φ	$\tau(\text{ns})$
Background	0.01	0.06	4.0	0.2	0.5
Target	0.1, 0.15	0.06	4.0	0.2	0.5
Emission Light	$\mu_{amf}(\text{mm}^{-1})$	$\mu_{ami}(\text{mm}^{-1})$	$\mu'_{sm}(\text{mm}^{-1})$	φ	$\tau(\text{ns})$
Background	0.01	0.02	1.0	0.2	0.5
Target	0.05, 0.1	0.02	1.0	0.2	0.5

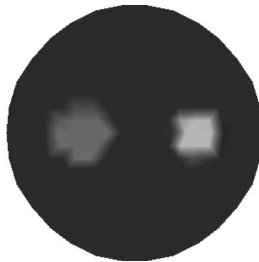


Fig. 8. Simulated phantoms for FMT of double target phantom.

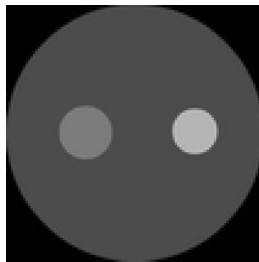


Fig. 9. Model of prior image of double target phantom.

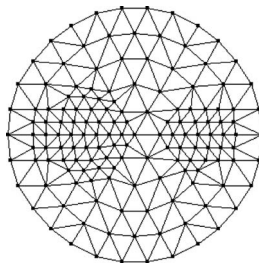


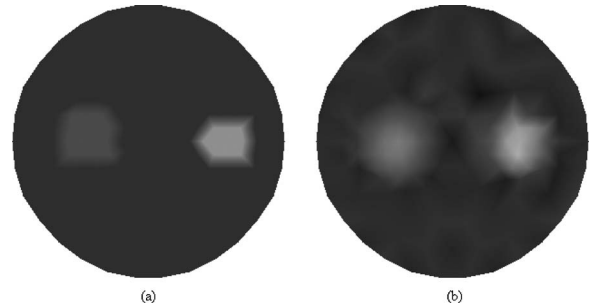
Fig. 10. Adaptively refined grid of double target phantom.

of the reconstructed target, while the multi-wavelength-measurement strategy can improve the quality of the target, especially in shape and location.

The quantitative comparisons of the performance among the reconstructed results based on different kinds of measurements are listed in Table 3. From this table, we can see that both the MSE and the averaged absolute value of relative error for the reconstructed image based

Table 5. Performance Comparison for Algorithms of Double Target Phantom

Performance	Proposed Algorithm	Traditional Method
MSE	2.049×10^{-4}	2.814×10^{-4}
Averaged absolute value of relative error	9.741×10^{-3}	1.311×10^{-2}
Computation time (s)	206	287

Fig. 11. Reconstructed image of absorption coefficient due to fluorophore μ_{axf} of double target phantom. (a) Proposed algorithm, and (b) traditional method.

on multi-wavelength measurement are smaller than those based on the single wavelength measurement. Thus, iteration with the measurements from different wavelengths in turn can improve the quality of image reconstruction and lead to more accurate reconstructed results.

B. Double Fluorescent Targets

In order to further validate our proposed algorithm for the case when there is more than one fluorescent target in the imaging area, simulated reconstruction is performed on the phantom as shown in Fig. 8, which contains two targets of different shapes representing the fluorescence centers. Table 4 outlines the optical and fluorescent parameters in different regions of the simulated phantom. Four sources and thirty detectors are used in the following simulation.

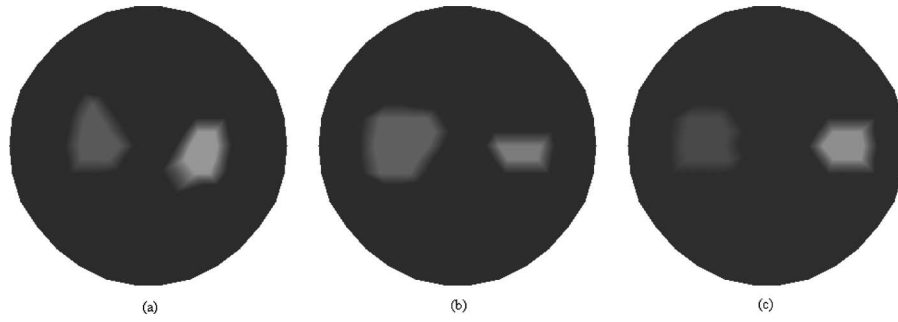


Fig. 12. Reconstructed image of absorption coefficient due to fluorophore μ_{axf} of double target phantom. (a) With excitation light measurement, (b) with emission light measurement, and (c) with multi-wavelength measurement.

The image shown in Fig. 9 is employed as the prior image corresponding to Fig. 8. The grid with 148 nodes and 264 triangular elements is generated as shown in Fig. 10 for the inverse problem of FMT.

Figures 11(a) and 11(b) show the reconstructed images of μ_{axf} using the proposed algorithm and the traditional pixel-based reconstruction method, respectively. Reconstructed results indicate that for the case of two fluorescent targets, the proposed algorithm can also provide more exact locations of the anomalies. The reconstructed areas with high and low absorption coefficients are also more visually similar to the simulation model than those resulting from the traditional method. From Fig. 11(a), we can also see that the quality of the reconstructed area with the high absorption coefficient is better than that with the low absorption coefficient.

Table 5 summarizes the performance of the above two algorithms for comparison, which demonstrates that both the quality and the speed of reconstruction can be improved with the proposed algorithm. This may be because the proposed algorithm has significantly reduced the number of unknowns to be solved. Therefore, the proposed algorithm is also valid for such a case of two targets in image reconstruction.

Furthermore, reconstructed results of μ_{axf} for the simulated phantom shown in Fig. 8 with the two single and the multi-wavelength measurement are shown in Figs. 12(a)–12(c), respectively. Similar to the case of single target reconstruction, there also exist some errors in the re-

sulting position and shape of the targets when single wavelength measurements are used. This may be due to lack of enough information for reconstruction. However, the results can be improved as in Fig. 12(c) when multi-wavelength measurements are used, which is because more information is introduced into image reconstruction.

The quantitative comparisons of the performance among the reconstructed results based on different kinds of measurement are listed in Table 6. It can be seen that reconstruction with multi-wavelength measurement provides a better result than that with either excitation light or emission light measurements. Hence, the multi-wavelength measurement strategy can improve the accuracy of inverse solutions.

In order to investigate the impact of the termination criterion ε on the MSE, the relative error and the computation time in the proposed algorithm-simulated reconstructions are implemented using our proposed algorithm with different values of ε . The results for the two fluorescent targets are shown in Table 7. From this table, we can see that with the increment of ε , the MSE and the averaged absolute value of the relative error of the reconstructed results increase, while the computation time of the reconstruction process decreases. Simulated reconstructions of a single fluorescent target are also performed under different choices of ε , based on which similar conclusions can also be drawn. This means that increasing ε will accelerate the reconstruction process but result in a worse reconstruction.

Table 6. Performance Comparison for Reconstructed Results of Double Target Phantom Based on Different Kinds of Measurement

Performance	Reconstruction with excitation light measurement	Reconstruction with emission light measurement	Reconstruction with multi-wavelength measurement
MSE	2.416×10^{-4}	2.358×10^{-4}	2.049×10^{-4}
Averaged absolute value of relative error	1.154×10^{-2}	1.128×10^{-2}	9.741×10^{-3}

Table 7. Impact of ε on the Reconstruction Process

ε	0.02	0.06	0.10	0.14
MSE	1.712×10^{-4}	2.049×10^{-4}	2.281×10^{-4}	2.772×10^{-4}
Averaged absolute value of relative error	8.239×10^{-3}	9.741×10^{-3}	1.103×10^{-2}	1.304×10^{-2}
Computation time (s)	215	206	193	172

4. CONCLUSION

In this paper, a region-based reconstruction algorithm that can significantly reduce the number of unknowns involved in reconstruction for FMT is proposed. This algorithm is not to perform a pixel-based reconstruction, which is highly underdetermined and ill-posed, but instead to reconstruct the target regions and the background area with constant optical or fluorescent properties. The target areas are determined by searching for the nearest neighbor nodes. For the region-based reconstruction method, in which the unknowns can be significantly reduced, we propose to incorporate the Hessian matrix in the optimization to accelerate the reconstruction process. Additionally, we propose a multi-wavelength reconstruction strategy that employs the excitation and emission light measurements in turn for iterative computation. Simulation results demonstrate that the proposed algorithm can not only significantly accelerate the reconstruction process but also achieve reconstructed results with high accuracy.

ACKNOWLEDGMENTS

This research is supported by the National Natural Science Foundation of China (NSFC) No. 60871086, the Natural Science Foundation of Jiangsu Province China No. BK2008159, and China Scholarship Council (CSC), Hong Kong Polytechnic University (PolyU), and Australian Research Council (ARC) grants.

REFERENCES

- C. Balas, "Review of biomedical optical imaging—a powerful, non-invasive, non-ionizing technology for improving in vivo diagnosis," *Meas. Sci. Technol.* **20**, 1–12 (2009).
- C. T. Xu, J. Axelsson, and S. Andersson-Engels, "Fluorescence diffuse optical tomography using upconverting nanoparticles," *Appl. Phys. Lett.* **94**, 251107–251107-3 (2009).
- R. B. Schulz, A. Ale, A. Sarantopoulos, M. Freyer, E. Soehngen, M. Zientkowska, and V. Ntziachristos, "Hybrid system for simultaneous fluorescence and x-ray computed tomography," *IEEE Trans. Med. Imaging* **29**, 465–473 (2010).
- V. Ntziachristos, "Fluorescence molecular imaging," *Annu. Rev. Biomed. Eng.* **8**, 1–33 (2006).
- A. B. Milstein, K. J. Webb, and C. A. Bouman, "Estimation of kinetic model parameters in fluorescence optical diffusion tomography," *J. Opt. Soc. Am. A* **22**, 1357–1368 (2005).
- F. Gao, H. Zhao, Y. Tanikawa, and Y. Yamada, "A linear, featured-data scheme for image reconstruction in time-domain fluorescence molecular tomography," *Opt. Express* **14**, 7109–9124 (2006).
- R. Roy, A. B. Thompson, A. Godavarty, and E. M. Sevick-Muraca, "Tomographic fluorescence imaging in tissue phantoms: a novel reconstruction algorithm and imaging geometry," *IEEE Trans. Med. Imaging* **24**, 137–154 (2005).
- A. Soubret, J. Ripoll, and V. Ntziachristos, "Accuracy of fluorescent tomography in the presence of heterogeneities: study of the normalized Born ratio," *IEEE Trans. Med. Imaging* **24**, 1377–1386 (2005).
- Y. Zhai and S. A. Cummer, "Fast tomographic reconstruction strategy for diffuse optical tomography," *Opt. Express* **17**, 5285–5297 (2009).
- M. E. Kilmer, E. L. Miller, D. A. Boas, D. H. Brooks, C. A. DiMarzio, and R. J. Gaudette, "Direct object localization and characterization from diffuse photon density wave data," *Proc SPIE* **3597**, 45–54 (1999).
- V. Kolehmainen, S. R. Arridge, W. R. B. Lionheart, M. Vauhkonen, and J. P. Kaipio, "Recovery of region boundaries of piecewise constant coefficients of an elliptic PDE from boundary data," *Inverse Probl.* **15**, 1375–1391 (1999).
- A. D. Klose, V. Ntziachristos, and A. H. Hielscher, "The inverse source problem based on the radiative transfer equation in optical molecular imaging," *J. Comput. Phys.* **202**, 323–345 (2005).
- H. K. Kim and A. Charette, "A sensitivity function-based conjugate gradient method for optical tomography with the frequency-domain equation of radiative transfer," *J. Quant. Spectrosc. Radiat. Transf.* **104**, 24–39 (2007).
- T. Tarvainen, M. Vauhkonen, and S. R. Arridge, "Gauss-Newton reconstruction method for optical tomography using the finite element solution of the radiative transfer equation," *J. Quant. Spectrosc. Radiat. Transf.* **109**, 2767–2778 (2008).
- F. Fedele, M. J. Eppstein, J. P. Laible, A. Godavarty, and E. M. Sevick-Muraca, "Fluorescence photon migration by the boundary element method," *J. Comput. Phys.* **210**, 1–24 (2005).
- A. P. Gibson, J. C. Hebden, and S. R. Arridge, "Recent advances in diffuse optical imaging," *Phys. Med. Biol.* **50**, R1–R43 (2005).
- S. R. Arridge, H. Dehghani, M. Schweiger, and E. Okada, "The finite element model of the propagation of light in scattering media: A direct method for domains with non-scattering regions," *Med. Phys.* **27**, 252–264 (2000).
- A. J. Chaudhari, F. Darvas, J. R. Bading, R. A. Moats, P. S. Conti, D. J. Smith, S. R. Cherry, and R. M. Leahy, "Hyperspectral and multispectral bioluminescence optical tomography for small animal imaging," *Phys. Med. Biol.* **50**, 5421–5441 (2005).
- S. R. Arridge and J. C. Schotland, "Optical tomography: forward and inverse problems," *Inverse Probl.* **25**, 1–59 (2009).
- A. D. Klose and A. H. Hielscher, "Quasi-Newton methods in optical tomographic image reconstruction," *Inverse Probl.* **19**, 387–409 (2003).
- A. Adler, T. Dai, and W. R. B. Lionheart, "Temporal image reconstruction in electrical impedance tomography," *Physiol. Meas.* **28**, S1–S11 (2007).
- J. R. Magnus and H. Neudecker, *Matrix Differential Calculus with Applications in Statistics and Econometrics*, Wiley Series in Probability and Statistics (Wiley, 1988).
- R. Roy, A. Godavarty, and E. M. Sevick-Muraca, "Fluorescence-enhanced optical tomography using referenced measurements of heterogeneous media," *IEEE Trans. Med. Imaging* **22**, 824–836 (2003).
- A. Y. Bluestone, M. Stewart, J. Lasker, G. S. Abdoulaev, A. H. Hielscher, "Three-dimensional optical tomographic brain imaging in small animals, part 1: hypercapnia," *J. Biomed. Opt.* **9**, 1046–1062 (2004).
- S. Walrand, F. Jamar, and S. Pauwels, "Improved solution for ill-posed linear systems using a constrained optimization ruled by a penalty: evaluation in nuclear medicine tomography," *Inverse Probl.* **25**, 1–17 (2009).
- C. Panagiotou, S. Somayajula, A. P. Gibson, M. Schweiger, R. M. Leahy, and S. R. Arridge, "Information theoretic regularization in diffuse optical tomography," *J. Opt. Soc. Am. A* **26**, 1277–1290 (2009).
- A. Joshi, W. Bangerth, and E. M. Sevick-Muraca, "Adaptive finite element based tomography for fluorescence optical imaging in tissue," *Opt. Express* **12**, 5402–5417 (2004).